ORIGINAL PAPER

A macro-element for incompressible finite deformations based on a volume averaged deformation gradient

E. F. I. Boerner · P. Wriggers

Abstract A three-dimensional 8-node brick continuum finite element formulation for incompressible finite elasticity is presented. The core idea is to introduce a substructure consisting of eight sub-elements inside each finite element, further referred to as macro-element. For each of the sub-elements, the deformation is averaged. The weak form for each sub-element is based on the Hu-Washizu principle. The response of each sub-element is assembled and projected onto the eight external nodes of the macro-element. The introduction of deformable sub-elements in case of incompressible elasticity has two major advantages. Firstly, it is possible to suppress locking by evaluating the volumetric part of the response only in the macro-element instead of in each of the sub-elements. Secondly, no integration is necessary due to the use of averaged deformations on the sub-element level. The idea originates from the Cosserat point element developed in Nadler and Rubin (Int J Solids Struct 40:4585–4614, 2003). A consistent transition between the Cosserat point macro-element and a displacement macro-element formulation using a kinematical description from the enhanced strain element formulation (Flanagan, Belytschko in Int J Numer Methods Eng 17:679–706, 1981) or (Belytschko et al. in Comput Methods Appl Mech Eng 43:251–276, 1984) and the principle of Hu-Washizu is presented. The performance is examined by means of numerical examples.

Keywords Finite element technology · Finite elasticity · Incompressibility

E. F. I. Boerner (✉) · P. Wriggers
Institute of Mechanics and Computational Mechanics,
Leibniz University of Hannover, 30167 Hannover, Germany
e-mail: boerner@ibnm.uni-hannover.de

P. Wriggers
e-mail: wriggers@ibnm.uni-hannover.de

1 Introduction

In structural analysis, many applications involve deformations which are associated with large strains. Furthermore, problems with large elastic strains are often constrained by the incompressibility of the material, as it is the case for rubber. Due to their simple geometry, three-dimensional 8-node brick elements are widely used in such applications.

It is well known that the presence of incompressibility leads to the so called "locking" phenomenon in case of a discretization with standard displacement elements, see [4]. Several methods to circumvent this problem have been developed. These are either reduced integration techniques, see e.g. [5], or mixed methods, [6] or [7]. In some approaches rank deficiency of underintegrated elements which then leads to hourglassing is bypassed by stabilization techniques, see e.g. [3,8,9] or [10]. In the pioneering works, [7] for the linear case or [11] for the nonlinear case, a family of elements has been developed, which is based on the Hu-Washizu variational principle. These elements are extensions of the incompatible QM6 element developed by [12]. They do not seem to have any rank deficiency and perform well in bending situations as well as in the case of incompressibility. Thus, these elements have general applicability. For geometrically linear analysis, [13] proposed a similar incompatible quadrilateral element that utilizes a second order Taylor series expansion of element basis functions in the physical coordinates. The element is designated QS6. This element was formulated for finite elastic strains in [14].

In the present paper, a finite element formulation for a three-dimensional 8-node brick element for incompressible materials is derived. It is called incompressible macro-element (MEI). The MEI makes use of a special version of the principle of Hu-Washizu to derive the underlying equations for the element construction. The main idea of

this formulation is to use an averaged deformation gradient which is also described within the Cosserat theory, see e.g. [1,15,16] or [17]. Using only the averaged deformation gradient, however, would immediately yield hourglassing modes if no additional stabilization is applied.

Therefore, a substructure consisting of eight sub-elements is introduced and the averaged deformation gradient is evaluated in each of the sub-elements. The introduction of a substructure has been proposed by e.g. [18], who describe a triangular element in which a 6-node triangle is constructed from four 3-node triangles with linear displacement fields each and a continuous linear strain field over the assemblage. This element is called composite triangular element. In [19], the finite element formulation proposed in [18] is examined together with the development of different types of triangular composite elements, one of them consisting e.g. of three 4-node quadrilaterals with one internal node. The composite element approach is extended to a three-dimensional formulation for tetrahedral composite finite elements in [20]. During the course of a collaboration on the Cosserat point element between the University of Hannover and the Technion, sponsored by the German Israel Foundation (GIF), [21] introduced the notion of a macro-element for the construction of the substructure in the 8-node brick-element. As opposed to [18,19] who introduce additional nodes on the element edges visible to the neighbour elements, the number of nodes that are visible to neighbour elements in case of the macro-element approach remains eight. Resistance to inhomogeneous modes of deformation, e.g. hourglassing of the macro-element, is obtained by modeling each sub-element using a volume averaged deformation gradient. The element proposed by [21] is formulated based on the Cosserat point approach. Here, a continuum approach using a Hu-Washizu functional will be applied to construct the element.

The response of each sub-element is assembled and projected onto the external nodes. In the special incompressible case, only the distortional part of the deformation is evaluated on the sub-element level while the volumetric part is only once computed on the external macro-element level. This avoids locking due to incompressibility. The formulation is compared with existing formulations by means of numerical examples.

2 Variational formulation

This section will provide the general nonlinear version of the variational formulation used to determine the respective quantities on both the sub-element and the macro-element level. The development of the nonlinear version of the macro-element is based on a multiple use of a general mixed variational principle. As shown in [11], the Hu-Washizu principle can be used as a point of departure for the develop-

ment of enhanced finite elements. Furthermore, [22] shows how averaged quantities can be incorporated in a variational formulation as a basis for finite element development. Again the principle of Hu-Washizu is applied.

2.1 Hu-Washizu variational formulation using the averaged deformation gradient

Since we want to base our finite element on the formulation of an averaged deformation gradient, the Hu- Washizu principle is formulated here first in terms of the deformation $\boldsymbol{\varphi}$, the averaged deformation gradient $\bar{\boldsymbol{F}}$ and the symmetric part of the first Piola–Kirchhoff stress tensor $\boldsymbol{P}$

$$\Pi(\boldsymbol{\varphi}, \bar{\boldsymbol{F}}, \boldsymbol{P}) = \int_{\mathcal{B}_0} \left(\Psi(\bar{\boldsymbol{F}}) + \boldsymbol{P} \cdot (\boldsymbol{F}(\boldsymbol{\varphi}) - \bar{\boldsymbol{F}}) \right) \, \mathrm{d}V$$
$$- \int_{\mathcal{B}_0} \boldsymbol{\varphi} \cdot \rho_0 \hat{\boldsymbol{b}} \, \mathrm{d}V - \int_{\partial \mathcal{B}_{0\sigma}} \boldsymbol{\varphi} \cdot \hat{\boldsymbol{t}} \, \mathrm{d}A \quad . \quad (1)$$

Here, Π is the elastic potential and $\boldsymbol{F}$ is the deformation gradient. The strain energy density function is denoted by Ψ, $\mathcal{B}_0$ ist the domain of $\mathcal{B}$ in the initial configuration. The initial volume is denoted V and A describes the surface of $\mathcal{B}_0$, $\partial \mathcal{B}_{0\sigma}$ is the Neumann boundary. The term $\rho_0 \hat{\boldsymbol{b}}$ is related to the body forces and the surface integral containing $\hat{\boldsymbol{t}}$ is associated with the prescribed traction loads. For simplicity, the last two terms will be summarized under the expression for the external loads P_{EXT}. The deformation gradient $\boldsymbol{F}(\boldsymbol{\varphi})$ is a function of the deformation $\boldsymbol{\varphi}$. The averaged deformation gradient $\bar{\boldsymbol{F}}$ is defined by the variation of the Hu-Washizu principle

$$\int_{\mathcal{B}_0} \boldsymbol{P} \cdot \operatorname{Grad} \boldsymbol{\eta} \, \mathrm{d}V - \delta P_{\mathrm{EXT}} = 0$$
$$\int_{\mathcal{B}_0} \delta \bar{\boldsymbol{F}} \cdot \left(-\boldsymbol{P} + \frac{\partial \Psi}{\partial \bar{\boldsymbol{F}}} \right) \, \mathrm{d}V = 0 \quad (2)$$
$$\int_{\mathcal{B}_0} \delta \boldsymbol{P} \cdot \left(\boldsymbol{F}(\boldsymbol{\varphi}) - \bar{\boldsymbol{F}} \right) \, \mathrm{d}V = 0,$$

where $\boldsymbol{\eta}$ is the virtual displacement field. Under the assumption that $\bar{\boldsymbol{F}}$ is constant within a domain in the initial configuration, one obtains

$$\bar{\boldsymbol{F}} = \frac{1}{V} \int_{\mathcal{B}_0} \boldsymbol{F}(\boldsymbol{\varphi}) \, \mathrm{d}V. \quad (3)$$

This is equivalent to defining $\bar{\boldsymbol{F}}$ as the volume average of the deformation gradient within a finite element, see also [15]. Additionally, one deduces from $(2)_2$ the constitutive equation

$$\boldsymbol{P} = \bar{\boldsymbol{P}} = \frac{\partial \Psi}{\partial \bar{\boldsymbol{F}}} = \frac{\partial \Psi}{\partial \boldsymbol{F}} \bigg|_{\boldsymbol{F} = \bar{\boldsymbol{F}}}, \quad (4)$$

which yields a constant stress field within the domain. Thus, Eq. (2)$_1$ can be written as

$$\bar{P} \cdot \int_{\mathcal{B}_0} \mathrm{Grad}\,\eta\,\mathrm{d}V - \delta P_{EXT} = 0. \tag{5}$$

With

$$\delta \bar{F} = \frac{1}{V} \int_{\mathcal{B}_0} \mathrm{Grad}\,\eta\,\mathrm{d}V, \tag{6}$$

we finally get

$$V\,\bar{P} \cdot \delta\bar{F} - \delta P_{EXT} = 0. \tag{7}$$

Under the assumption that $\bar{F}$ is constant, the kinematics, the constitutive equation as well as the weak form of equilibrium can be expressed by constant stress and strain measures and the integral in the weak form of equilibrium can be eliminated. The weak form of equilibrium can now be expressed in the initial configuration by aid of the standard transformation $\bar{P} = \bar{F}\bar{S}$. Here, $\bar{S}$ is the volume averaged second PIOLA- KIRCHHOFF stress tensor. One arrives at

$$V\bar{S} \cdot \frac{1}{2}\left(\bar{F}^T \delta\bar{F} + \delta\bar{F}^T \bar{F}\right) - \delta P_{\mathrm{EXT}} = 0. \tag{8}$$

The strain energy function in (1) can now be written in terms of $\bar{C} = \bar{F}^T\bar{F}$ as $\Psi(\bar{C})$. Here, C is the right CAUCHY- GREEN tensor and $\bar{C}$ will be denoted volume averaged right CAUCHY- GREEN tensor.

2.2 Constitutive equations

A hyperelastic Neo-HOOKE material using a volumetric-deviatoric split is used. The strain energy density function Ψ as proposed in [23] is given by

$$\Psi(\bar{C}) = \frac{\mu}{2}\left(I_{\bar{\bar{C}}} - 3\right) + g(\bar{J}), \quad I_{\bar{\bar{C}}} = \mathrm{tr}\,(\bar{\bar{C}}), \tag{9}$$

where $\bar{J} = \det\bar{F}$ denotes the JACOBIan of the averaged deformation gradient, μ is the shear modulus and

$$\bar{\bar{C}} = \bar{\bar{F}}^T \cdot \bar{\bar{F}}, \quad \bar{\bar{F}} = \bar{J}^{-1/3}\bar{F}. \tag{10}$$

The volumetric part of the strain energy function $g(J)$ can be chosen from

$$g(\bar{J}) = \begin{cases} \dfrac{K}{\beta^2}\left(\dfrac{1}{\bar{J}^\beta} - 1 + \beta\ln\bar{J}\right) \\[2mm] \dfrac{K}{2}\left(\bar{J} - 1\right)^2 \\[2mm] \dfrac{K}{2}\ln^2\bar{J} \end{cases}, \tag{11}$$

where K is the small deformation bulk modulus and β is a material parameter that controls nonlinearity of the volumetric part of the strain energy function $g(J)$. The volume

averaged second PIOLA- KIRCHHOFF stress tensor $\bar{S}$ for this strain energy density function is given by

$$\bar{S} = \mu\bar{J}^{-2/3}\left(1 - \frac{1}{3}\mathrm{tr}\,(\bar{C})\bar{C}^{-1}\right) + \bar{J}\frac{\partial g}{\partial\bar{J}}\bar{C}^{-1}. \tag{12}$$

The KIRCHHOFF stress tensor τ is obtained by a push forward, such that

$$\bar{\tau} = \bar{F} \cdot \bar{S} \cdot \bar{F}^T = \mu\bar{J}^{-2/3}\left(\bar{b} - \frac{1}{3}\mathrm{tr}\,(\bar{b})\mathbf{1}\right) + \bar{J}\frac{\partial g}{\partial\bar{J}}\mathbf{1}, \tag{13}$$

where $\bar{b} = \bar{F}\bar{F}^T$ is the volume averaged left CAUCHY- GREEN tensor. With the following definition of the CAUCHY stress tensor σ in the current configuration of the domain $\mathcal{B}_t$

$$\int_{\mathcal{B}_t}\sigma\,\mathrm{d}v = \int_{\mathcal{B}_t}\frac{1}{J}\tau\,\mathrm{d}v = \int_{\mathcal{B}_0}\tau\,\mathrm{d}V, \tag{14}$$

the corresponding volume averaged CAUCHY stress tensor $\bar{\sigma}$ is obtained to

$$v_t\bar{\sigma} = V_0\bar{\tau}. \tag{15}$$

Here, V_0 and v_t denote the volume in the initial and current configuration respectively.

3 Theory macro-element

This section provides a brief summary of the macro-element theory. The core idea of the macro-element is to introduce a substructure of eight sub-elements. Figure 1 shows the macro-element with the external nodes (1,…,8) as well as the sub-elements, for which the interim internal nodes (9,…,27) are introduced.

Note, that the nodes 1,…,8 will be called external nodes in the following. All measures that are given for these nodes only will be indexed $_{\mathrm{ext}}$. The interim nodes 9,…,27 are called internal nodes. They are not visible to the neighbour elements. Together, the external and internal nodes are called all nodes and measures given for all nodes will be indexed $_{\mathrm{all}}$. The notion macro-element is used for the idea and the element formulation itself.

3.1 Discrete kinematics of the macro-element

The macro-element formulation presented here uses a trilinear appoximation for the geometry. The element geometry is obtained by use of a standard isoparametric mapping

$$X = \sum_{I=1}^{8} N^I(\xi)X_I, \quad x = \sum_{I=1}^{8} N^I(\xi)x_I, \tag{16}$$

where X_I and x_I refer to the nodal coordinates of the eight external nodes in the initial and current configuration respectively. N^I denotes a standard LAGRANGE shape function for
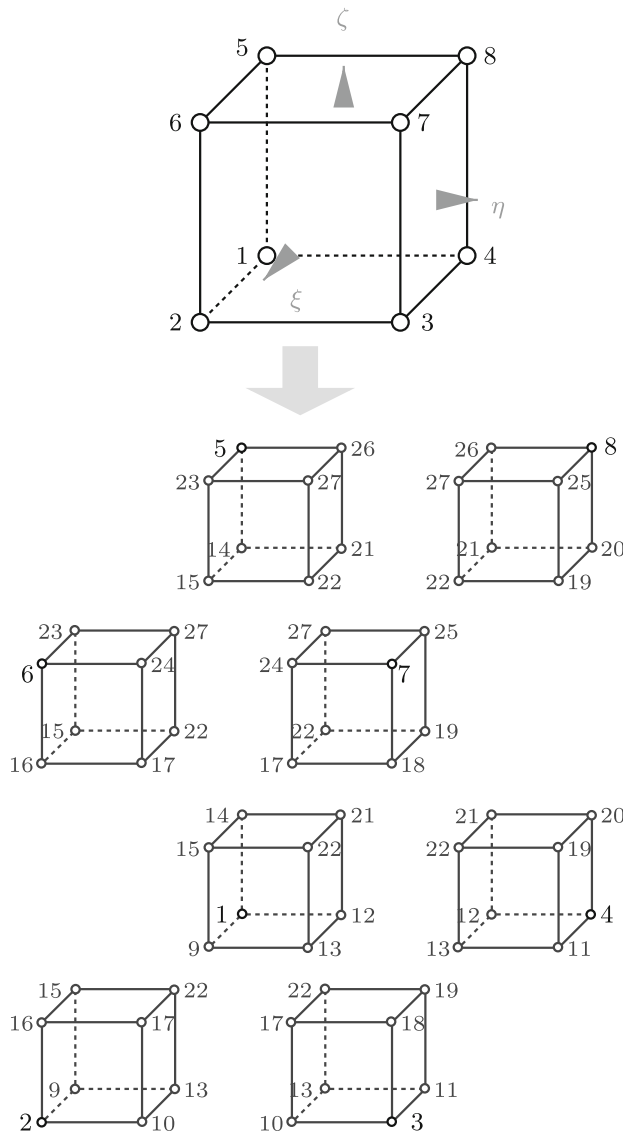
Fig. 1 Macro-element and sub-elements including node numbers in the reference configuration $P_\square$

the 8-node brick-element defined in the reference configuration $P_\square$ depicted in Fig. 1. The shape functions are given by

$$N^I(\boldsymbol{\xi}) = \frac{1}{8}(1 - \xi_I\xi)(1 - \eta_I\eta)(1 - \zeta_I\zeta) ,$$
$$(I = 1, \ldots, 8). \qquad (17)$$

Here, ξ, η and ζ are the coordinates in the reference configuration and ξ_I, η_I and ζ_I are the nodal coordinates in the reference configuration.

The introduction of sub-elements naturally calls for additional internal nodes as indicated in Fig. 1. Their position is prescribed in the reference configuration. Although the internal nodes initially can be arbitrarily located on the edges, surfaces and the interior of the macro-element, they are chosen to be the respective midpoints in the reference configuration.

It can be shown, that a fixation of the reference coordinates of the internal nodes preserves hyperelasticity within the framework of the approximation for the macro-element formulation. The coordinates of an internal node K in the reference configuration are denoted by $\boldsymbol{\xi}_K$, such that the nodal positions of the internal nodes X_K in the initial and $\boldsymbol{x}_K$ current configuration read

$$X_K = \sum_{I=1}^{8} N^I(\boldsymbol{\xi}_K)X_I , \quad \boldsymbol{x}_K = \sum_{I=1}^{8} N^I(\boldsymbol{\xi}_K)\boldsymbol{x}_I ,$$
$$(K = 9, \ldots, 27) . \qquad (18)$$

As the positions of the internal nodes are partially fixed due to the restriction that e.g. node 9 has to be located on the edge between node 1 and 2, the number of unknowns for the determination of the position of the internal nodes reduces significantly. Equation (18) can be simplified by introducing the transformation matrix $\boldsymbol{T}$ according to

$$X_{\text{all}} = \boldsymbol{T} \cdot X_{\text{ext}} . \qquad (19)$$

Here, X_{all} is a 27×3 matrix containing all nodal coordinates and X_{ext} is a 8×3 matrix containing the nodal coordinates of the eight external nodes. $\boldsymbol{T}$ is given in appendix A, where the internal nodes $(9,\ldots,27)$ are assumed to be located at the midpoints of the edges, surfaces and the interior respectively.

3.2 Averaged deformation gradient

The introduction of the internal nodes and the sub-elements is a prerequisite for the determination of the element response: the residual vector and the tangent stiffness matrix. For both, strains and stresses are needed. Here, a Neo-HOOKE material will be used, as introduced earlier in Sect. 2.2. In order to evaluate the stresses, the averaged deformation gradient $\bar{\boldsymbol{F}}$ has to be determined according to Eq. (3). This yields

$$\bar{\boldsymbol{F}} = \boldsymbol{1} + \int_{\mathcal{B}_{0,sub}} \text{Grad}\, \boldsymbol{u}^h \, dV$$
$$= \boldsymbol{1} + \sum_{I=1}^{8} \boldsymbol{u}_I \otimes \int_{\mathcal{B}_{0,sub}} \text{Grad}\, N^I \, dV . \qquad (20)$$

Above, $\mathcal{B}_0$ denotes any domain in the initial configuration. Obviously, the averaged deformation gradient makes use of the averaged gradient of the shape functions N^I in the initial configuration of each sub-element. These averaged gradients can be determined in different ways. One is the evaluation via standard numerical integration with GAUSS points in each sub-element. Here, eight GAUSS points are used. Alternatively, the evaluation of the integral for the averaged deformation gradient can be performed analytically by use of the kinematics of an enhanced strain element as introduced in [2] or [3]. Then, the TAYLOR expansion of the shape

functions together with the definition of so-called $\boldsymbol{\gamma}$-vectors yields expressions for the averaged deformation gradient $\bar{\boldsymbol{F}}$. For more detailed information, see e.g. [8,9].

$$\bar{\boldsymbol{F}} = \frac{1}{V} \int_{\mathcal{B}_0} \boldsymbol{x}_{\text{ext}}^T \cdot \left(\boldsymbol{N}_{\text{lin},\boldsymbol{\xi}} \cdot \boldsymbol{J}^{-1} \right)_{\boldsymbol{\xi}=\boldsymbol{\xi}_0} \, \mathrm{d}V$$

$$+ \frac{1}{V} \int_{\mathcal{B}_0} \boldsymbol{x}_{\text{ext}}^T \cdot \left(\sum_{k=1}^{3} \frac{\partial N_\gamma}{\partial \xi^k} \otimes \boldsymbol{G}^k \right) \mathrm{d}V \ . \tag{21}$$

Here, $\boldsymbol{N}_{\text{lin},\boldsymbol{\xi}}$ is the gradient of a vector containing the part of all shape functions that is of linear or lower order with respect to the reference coordinates $\boldsymbol{\xi}$. $\boldsymbol{N}_\gamma$ is a vector containing the part of the shape functions that is of higher than linear order. $\boldsymbol{J}$ is the JACOBIan and $\boldsymbol{G}^k$ denotes the contravariant convective base vectors for the initial configuration.

$$\boldsymbol{J} = \frac{\partial \boldsymbol{X}}{\partial \boldsymbol{\xi}} , \quad \boldsymbol{G}_k = \frac{\partial \boldsymbol{X}}{\partial \xi^k}$$

$$\boldsymbol{N} = \boldsymbol{N}_{\text{lin}} + \boldsymbol{N}_\gamma = (N^1, \dots, N^8)^T \ . \tag{22}$$

Another way to evaluate the averaged deformation gradient exists. It is given in the theory of a Cosserat point, see e.g. [1,15,16] or [17]. Here, the expression for $\bar{\boldsymbol{F}}$ above can be directly translated into the averaged deformation gradient used in the so-called Cosserat point element.

3.3 Evaluation and projection

The element quantities such as the tangent stiffness matrix or the residual vector can now be evaluated by use of the averaged deformation gradient described above and the constitutive equations given in Sect. 2.2. The idea of the macro-element is to evaluate only the homogeneous part of the deformation but to do this in each sub-element. Hence, $\mathcal{B}_0$ in Eq. (20) is replaced by each sub-element domain. The incompressible macro-element additionally distinguishes the homogeneous deviatoric and the homogeneous volumetric part of the deformation, as the latter is not evaluated in each sub-element but only once on the external macro-element level. The sub-element and macro-element quantities are then assembled to all nodes (1,…,27), yielding e.g. the 27×3 residual vector $\boldsymbol{r}_{\text{all}}$. Then, the internal nodal quantities in the unprojected residual vector $\boldsymbol{r}_{\text{all}}$ are projected onto the external nodes yielding the final residual vector $\boldsymbol{r}_{\text{ext}}$. Again, the transformation matrix $\boldsymbol{T}$ can be used for this projection, which equals a condensation of information. The projected final element residual vector $\boldsymbol{r}_{\text{ext}}$ is an 8×3 vector obtained by

$$\boldsymbol{r}_{\text{ext}} = \boldsymbol{T}^T \cdot \boldsymbol{r}_{\text{all}} \ . \tag{23}$$

4 Numerical examples

The proposed finite element formulation presented above is tested by numerical examples concerning a possible rank deficiency, its general performance and its robustness. The results of the incompressible macro-element (MEI) are compared with the results of a standard displacement element (Q1) and with the results of the mixed Q1P0 element formulation designed for incompressible problems.

4.1 Linearized eigenvalue analysis

The eigenvalues of the unrestrained tangent stiffness matrix are examined in the initial elastic configuration for a single element. This simulation aims to assess the performance of the incompressible macro-element. A ratio of $K/\mu = 10^9$ enforces the incompressibility constraint. The element shape is an undistorted cube with an edge length of $h = w = l = 2.0$. It is depicted in Fig. 2 together with the material properties.

The eigenvalues are given in Table 1. Naturally, six eigenvalues are associated with rigid body motions. They are equal to zero and therefore omitted. More results for the same test and different enhanced finite element formulations are given in [24].

All three element formulations have one very large eigenvalue. This eigenvalue corresponds to the hydrostatic mode which is associated with the incompressibility constraint. The Q1-element shows six additional very large eigenvalues which indicate the severe locking-behaviour of this element type. As expected, both the Q1P0- element as well as the incompressible macro-element exhibit only one eigenvalue approaching infinity as $K/\mu \to \infty$. The macro-element does not show any tendency to suffer from locking or rank deficiency and its formulation is apparently close to that of the Q1P0 element. It should be mentioned that the same test has been performed for a severely initially distorted element, which has been proposed by [24]. The results for the distorted element lead to the same conclusions as the results for the cubic element. Therefore, they are here not given in detail.
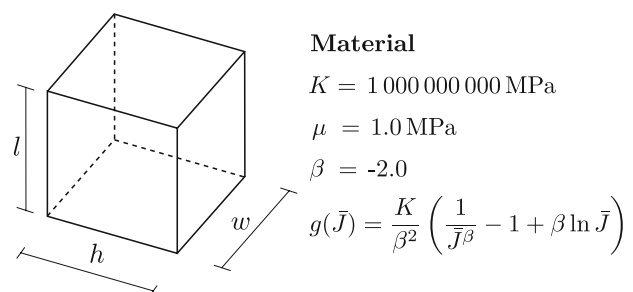

Fig. 2 Model eigenvalue analysis

Material

$K = 1\,000\,000\,000\,\text{MPa}$

$\mu = 1.0\,\text{MPa}$

$\beta = -2.0$

$g(\bar{J}) = \frac{K}{\beta^2} \left(\frac{1}{\bar{J}^\beta} - 1 + \beta \ln \bar{J} \right)$

Table 1 Results eigenvalue analysis in MPa: cubic element

Q1	Q1P0	MEI
3.3333E-01	3.3333E-01	3.3333E-01
3.3333E-01	3.3333E-01	3.3333E-01
1.0000E+00	3.7037E-01	3.3333E-01
1.0000E+00	3.7037E-01	5.0000E-01
1.0000E+00	3.7037E-01	5.0000E-01
1.3333E+00	5.5556E-01	6.6667E-01
2.0000E+00	5.5556E-01	6.6667E-01
2.0000E+00	5.5556E-01	6.6667E-01
2.0000E+00	1.0000E+00	1.0000E+00
2.0000E+00	1.0000E+00	1.0000E+00
2.0000E+00	1.0000E+00	1.0000E+00
1.1111E+08	1.3333E+00	2.0000E+00
1.1111E+08	2.0000E+00	2.0000E+00
1.1111E+08	2.0000E+00	2.0000E+00
6.6667E+08	2.0000E+00	4.0000E+00
6.6667E+08	2.0000E+00	4.0000E+00
6.6667E+08	2.0000E+00	4.0000E+00
3.0000E+09	3.0000E+09	3.0000E+09

4.2 Nearly incompressible block under compression

A standard test for the performance of a finite element formulation in case of incompressibility is the incompressible block under pressure depicted in Fig. 3. A parallelepiped shaped block of dimensions h, w and l is loaded with an equally distributed surface load q at its top center, while all the nodes on the top of the block are fixed in x_1- and x_2-direction. The bottom nodes are fixed in x_3-direction. Due to symmetry, only one quarter of the block is discretized and symmetric boundary conditions are applied at the inner symmetry surfaces. The boundary conditions are chosen according to a similar test in [9]. The geometry and the material properties as well as the applied load are given in Fig. 3. The convergence of the deflection w_P of point P in x_3-direction is compared for the different element formulations. Figure 4 depicts the unstructured meshes with $4 \times 4 \times 4$, $8 \times 8 \times 8$ and $16 \times 16 \times 16$ elements respectively. The surfaces of the elements in the loading zone remain square during mesh refinement. The incompressible macro-element converges as fast as the Q1P0-element. Already the coarsest mesh yields the correct results. As expected, the Q1 element locks. This test additionally shows that the incompressible macro-element does not experience problems for initially distorted meshes. The results for the convergence study are depicted in Fig. 5.

4.2.1 Robustness

In addition to the general performance, the robustness of the macro-element is compared to the robustness of the Q1P0
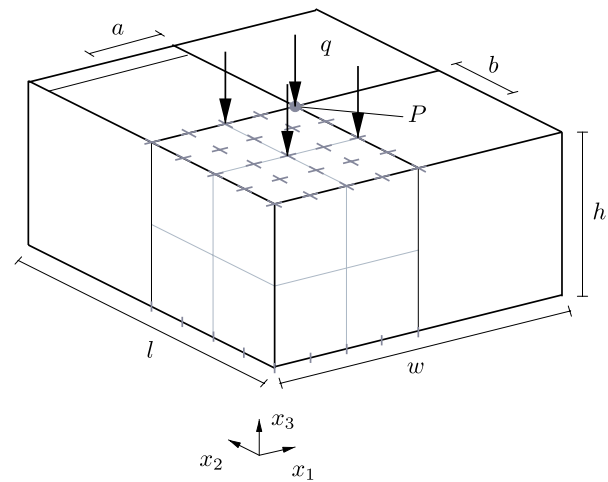
Geometry

$h = 50$ mm

$w = 100$ mm

$l = 100$ mm

$a = 25$ mm

$b = 24$ mm

Material

$K = 501$ MPa
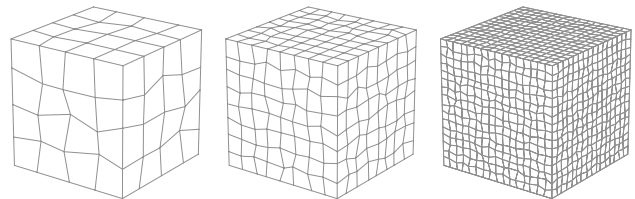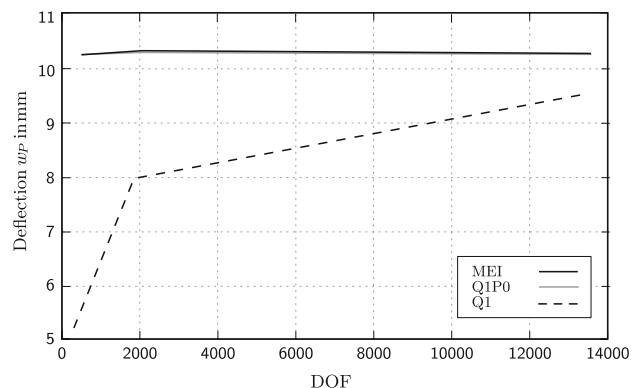
$\mu = 3.22296$ MPa

$\beta = -2.0$

$$g(\bar{J}) = \frac{K}{\beta^2} \left(\frac{1}{\bar{J}^\beta} - 1 + \beta \ln \bar{J} \right)$$

Load

$q = 3$ MPa

Fig. 3 Model of the nearly incompressible block

Fig. 4 Meshes incompressible block

Fig. 5 Results for the nearly incompressible block: convergence study for the vertical deflection w_P and the load $q = 3.0$ MPa
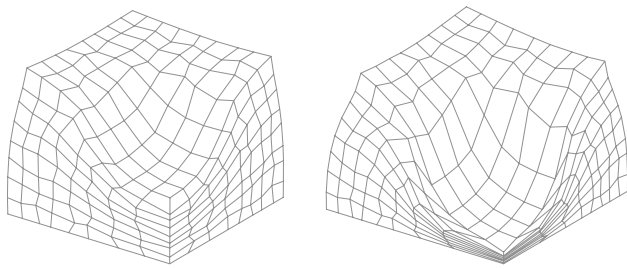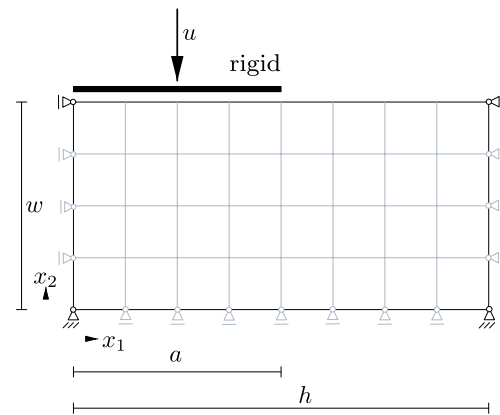
Fig. 6 Deformed meshes for the nearly incompressible block at $q = 10$ MPa and $q = 30$ MPa, $8 \times 8 \times 8$ elements

element. Both element formulations can be compressed up to very high loads. A picture of the deformed meshes for the discretization with $8 \times 8 \times 8$ elements at the load levels $q = 10.0$ MPa and $q = 30.0$ MPa is given for the macro-element in Fig. 6. The deformed meshes look the same for the Q1P0 element and the displacements are alike as well. Both element formulations are robust in this sense, although the macro-element shows the tendency to be more robust in the sense of larger load step sizes.

4.3 Indentation problem

The indentation problem is a compression test, which examines the robustness of the incompressibility algorithms for highly distorted meshes. A plane strain block of dimensions h, w (and $l = 1$ mm) is restricted on the left and right boundary in x_1-direction and at the bottom in x_2-direction. A uniform displacement is applied in x_2-direction at the top, which can be interpreted as a frictionless rigid plate that is pressed onto the body below as depicted in Fig. 7. Plane strain is incorporated by fixing all nodes in x_3-direction, one element is used in the x_3-direction. The geometry, boundary and load conditions are chosen according to [25–27]. The material properties differ from [25–27], where a MOONEY- RIVLIN material is used. Here, the material parameters are adopted to a Neo-HOOKEan material, they are given in Fig. 7. The convergence of this problem can become very unstable due to the immense deformation of the elements, especially the elements close to the edge of the rigid plate. $8 \times 4 (\times 1)$ elements are used for the discretization of this problem. Incompressibility is ensured by choice of a very high bulk modulus K, which leads to an ill-conditioning of the problem. The amount of compression that can be applied until failure varies for the different element types. Due to the fact that the total amount of deformation depends on time step size, Table 2 displays the results in terms of the relative displacement $\bar{u} = u/w$ in percent for different time step sizes. For a reasonably small time step size of dt $= 0.001$, the incompressible macro-element reaches a deformation level $\bar{u} = u/w = 24.0\%$, whereas the Q1P0 element reaches a deformation level of $\bar{u} = 22.6\%$. The reasons

Fig. 7 Model indentation problem

Geometry	Material
$h = 2$ mm	$K = 100\,000$ MPa
$w = 1$ mm	$\mu = 2.0$ MPa
$l = 1$ mm	
$a = 1$ mm	$g(J) = \dfrac{K}{\beta^2}\left(\dfrac{1}{\bar{J}} - 1 + \beta\ln\bar{J}\right)$

Table 2 Deformation level $\bar{u}$ in % using different time step sizes

dt	$\bar{u}_{\max}$ MEI	$\bar{u}_{\max} Q1P0$
0.005	6.0	3.5
0.002	21.2	22.6
0.001	24.0*	22.6

* Computations manually stopped due to unappropriate boundary conditions

for the failure of applying more displacements are different for both element formulations. While the computations using the Q1P0 element fail as soon as the element shape of the rightmost element underneath the rigid plate starts to become non-convex, the computations using incompressible macro-element are stopped manually at a deformation level af approximately $\bar{u} = 24\%$. This manual intervention is done due to the fact that the node at the rightmost edge of the rigid plate starts moving beyond one of the inner nodes. This is a consequence of the chosen boundary conditions. The unequal "failure" behaviour of the Q1P0 element and the MEI is illustrated by the deformed meshes depicted in Fig. 8 as well as the fact that computations with the Q1P0 element crash at the deformation level $\bar{u} = 22.6\%$. The deformed meshes already reveal that the incompressible macro-element behaves less stiff for this problem compared to the Q1P0 element. This can also be observed in the load-displacement curves in Fig. 9 depicting the total vertical force acting on the body in relation to the applied displacement level $\bar{u}$. The reaction forces of the Q1 element are not given in Fig. 9 as they quickly approach very large values. For $\bar{u} = 10\%$, the vertical force
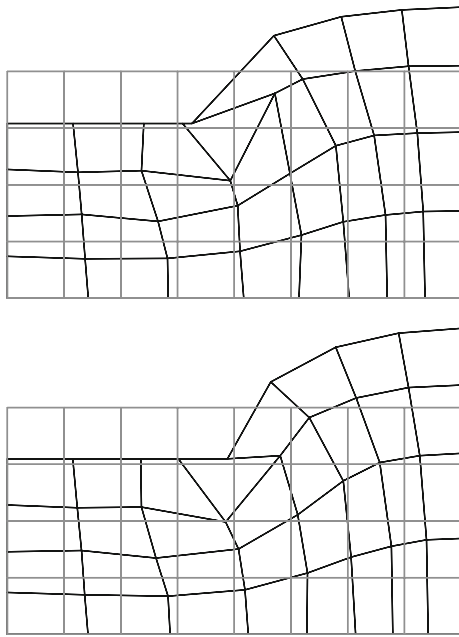
Fig. 8 Deformed meshes indentation problem: Macro-element at $\bar{u} = 23\%$ and Q1P0 element at $\bar{u} = 22.6\%$ indentation and $K = 100\,000\,\mathrm{MPa}$
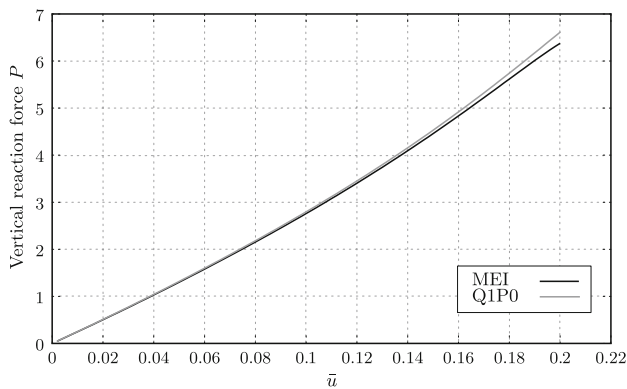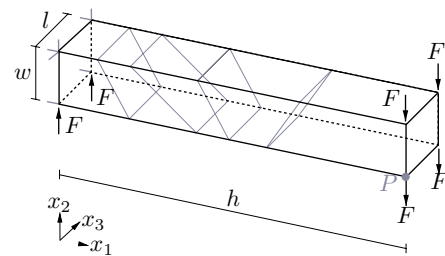

Fig. 9 Result indentation problem: load-displacement curve for an indentation equal to $\bar{u} = 20\%$ and $K = 100\,000\,\mathrm{MPa}$

P reaches a value of $P = 772\,\mathrm{N}$ and for $\bar{u} = 20\%$ a vertical load of $P = 1591\,\mathrm{N}$ is computed for the Q1 element.

4.4 Large rotation and deflection of a cantilever beam

This test examines the performance of the different element formulations in a situation which combines incompressibility and large deformations. A three-dimensional cantilever beam is loaded in bending and shear by way of a distributed shear force $4F$ at its end. The boundary and loading conditions as well as the dimensions of the beam and the material parameters are given in Fig. 10. They are chosen according to [27]. All nodes on the left boundary at $x_1 = 0$ are fixed in x_1-direction, where the bottom nodes are additionally loaded

Geometry	Material
$h = 10\,\mathrm{mm}$	$K = 1\,666\,666.67\,\mathrm{MPa}$
$w = 2\,\mathrm{mm}$	$\mu = 33.33\,\mathrm{MPa}$
$l = 1\,\mathrm{mm}$	$\beta = -2.0$
$h_B = 2/2/1/1/4\,\mathrm{mm}$	
$h_T = 1/1/2/3/3\,\mathrm{mm}$	

Load

$F = 1.5\,\mathrm{N}$ $\qquad g(\bar{J}) = \dfrac{K}{\beta^2}\left(\dfrac{1}{\bar{J}^\beta} - 1 + \beta \ln \bar{J}\right)$
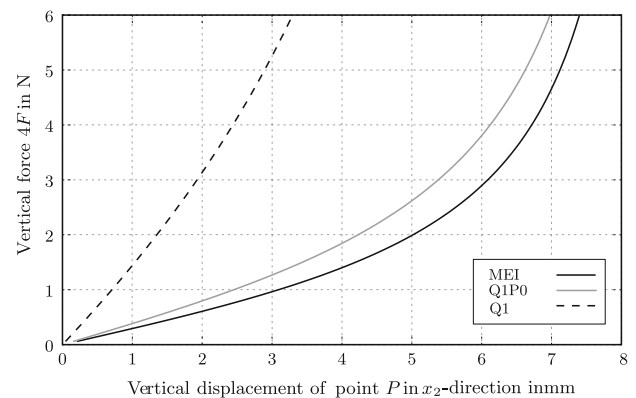
Fig. 10 Model cantilever beam

Fig. 11 Results cantilever beam: load-displacement curve for the vertical displacement in P

by the force F each. The top nodes at the left boundary are also fixed in x_2-direction, the front top node is fixed in all three directions. The initial mesh is also depicted in Fi. 10. The beam is divided into five elements, the bottom edges have the lengths h_B in x_1-direction, while the top edges have the lengths h_T in x_1-direction. The results for this test are given in Figs. 11 and 12. Both figures each show a load-displacement curve in point P for the different element formulations. Figure 11 plots the vertical displacement in x_2-direction, while Fig. 12 depicts the horizontal displacement in x_1-direction.

The deformed mesh can be seen exemplarily for the incompressible macro-elment in Fig. 13. The Q1P0 element behaves stiffer in bending compared to the incompressible macro-element. The final displacements are of the same magnitude as the displacements obtained in [27].
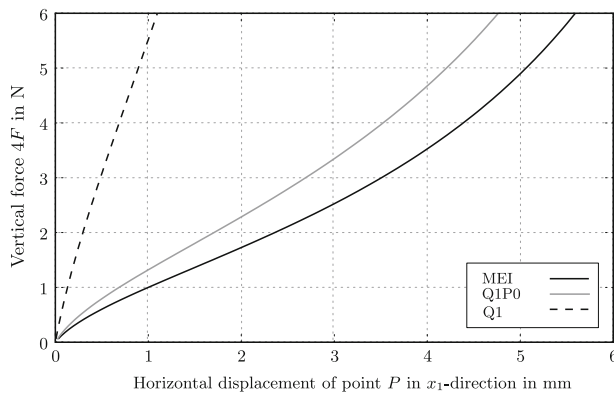
Fig. 12 Results cantilever beam: load-displacement curve for the horizontal displacement in P
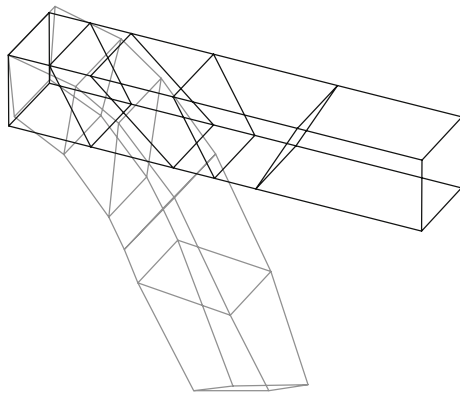

Fig. 13 Deformed mesh cantilever beam: MEI element, deformation scaling factor = 1.0

5 Conclusions

By aid of the HU- WASHIZU principle, it was possible to derive a consistent finite element formulation using volume averaged deformations. The macro-element idea is applied by introducing sub-elements and constructing projection algorithms for the kinematical and henceforth all relevant element measures. Incompressibility is incorporated by a decoupling of the averaged distortional deformation on the sub-element level and the volumetric part of the averaged deformation on the macro-element level. The performance of the incompressible macro-element that is constructed from the ideas described above is examined in a number of numerical tests to check for possible rank deficiency, locking behaviour, stability and robustness. The eigenvalue analysis reveals no rank deficiency. For the incompressible block test, neither locking nor problems with initially distorted meshes are observed. The incompressible macro-element exhibits a very robust behaviour, larger loadsteps can be used than for the Q1P0 element for the nearly incompressible block problem. The indentation problem shows another strength of the incompressible macro-element as it is insensitive to non-convexity of the element shapes. Additionally, the incompressible macro-element behaves slightly less stiff compared to the Q1P0 element for the indentation problem as indicated by the load-displacement curves. Additionally, the incompressible macro-element behaves better in bending, which is illustrated in the last example. Here, the incompressible macro-element captures the bending deformations better than the Q1P0 element, which reacts stiffer. The incompressible macro-element, finally, is a robust and efficient finite element formulation that can be used as an alternative to the well-known Q1P0 element for incompressible problems with moderate incompressibility.

6 Appendix

The transformation matrix $\boldsymbol{T}$ as introduced in Eq. (19) is given by

$$
\underline{T} =
\begin{bmatrix}
1 & 0 & 0 & 0 & 0 & 0 & 0 & 0 \\
0 & 1 & 0 & 0 & 0 & 0 & 0 & 0 \\
0 & 0 & 1 & 0 & 0 & 0 & 0 & 0 \\
0 & 0 & 0 & 1 & 0 & 0 & 0 & 0 \\
0 & 0 & 0 & 0 & 1 & 0 & 0 & 0 \\
0 & 0 & 0 & 0 & 0 & 1 & 0 & 0 \\
0 & 0 & 0 & 0 & 0 & 0 & 1 & 0 \\
0 & 0 & 0 & 0 & 0 & 0 & 0 & 1 \\
0.5 & 0.5 & 0 & 0 & 0 & 0 & 0 & 0 \\
0 & 0.5 & 0.5 & 0 & 0 & 0 & 0 & 0 \\
0 & 0 & 0.5 & 0.5 & 0 & 0 & 0 & 0 \\
0.5 & 0 & 0 & 0.5 & 0 & 0 & 0 & 0 \\
0.25 & 0.25 & 0.25 & 0.25 & 0 & 0 & 0 & 0 \\
0.5 & 0 & 0 & 0 & 0.5 & 0 & 0 & 0 \\
0.25 & 0.25 & 0 & 0 & 0.25 & 0.25 & 0 & 0 \\
0 & 0.5 & 0 & 0 & 0 & 0.5 & 0 & 0 \\
0 & 0.25 & 0.25 & 0 & 0 & 0.25 & 0.25 & 0 \\
0 & 0 & 0.5 & 0 & 0 & 0 & 0.5 & 0 \\
0 & 0 & 0.25 & 0.25 & 0 & 0 & 0.25 & 0.25 \\
0 & 0 & 0 & 0.5 & 0 & 0 & 0 & 0.5 \\
0.25 & 0 & 0 & 0.25 & 0.25 & 0 & 0 & 0.25 \\
0.125 & 0.125 & 0.125 & 0.125 & 0.125 & 0.125 & 0.125 & 0.125 \\
0 & 0 & 0 & 0 & 0.5 & 0.5 & 0 & 0 \\
0 & 0 & 0 & 0 & 0 & 0.5 & 0.5 & 0 \\
0 & 0 & 0 & 0 & 0 & 0 & 0.5 & 0.5 \\
0 & 0 & 0 & 0 & 0.5 & 0 & 0 & 0.5 \\
0 & 0 & 0 & 0 & 0.25 & 0.25 & 0.25 & 0.25
\end{bmatrix}
\tag{24}
$$

The first derivative of the volumetric part of the strain energy function is given by

$$
\frac{\partial g(\bar{J})}{\partial \bar{J}} =
\begin{cases}
\dfrac{K}{\beta}\left(-\dfrac{1}{\bar{J}^{\beta+1}} + \dfrac{1}{\bar{J}}\right) \\
K\left(\bar{J} - 1\right) \\
\dfrac{K}{\bar{J}}\ln\bar{J}
\end{cases}.
\tag{25}
$$

References

1. Nadler B, Rubin MB (2003) A new 3-d finite element for nonlinear elasticity using the theory of a Cosserat point. Int J Solids Struct 40:4585–4614
2. Flanagan DP, Belytschko T (1981) A uniform strain hexahedron and quadrilateral with orthogonal hourglass control. Int J Numer Methods Eng 17:679–706
3. Belytschko T, Ong JSJ, Liu WK, Kennedy JM (1984) Hourglass control in linear and nonlinear problems. Comput Methods Appl Mech Eng 43:251–276
4. Hughes TJR (1987) The finite element method. Prentice Hall, Englewood Cliffs
5. Malkus DS, Hughes TJR (1978) Mixed finite element methods - reduced and selective integration techniques: a unification of concepts. Comput Methods Appl Mech Eng 15:63–81
6. Pian THH, Sumihara K (1984) Rational Approach for assumed stress finite elements. Int J Numer Methods Eng 20:1685–1695
7. Simo JC, Rifai MS (1990) A class of assumed strain methods and the method of incompatible modes. Int J Numer Methods Eng 29:1595–1638
8. Belytschko T, Bindemann LP (1986) Assumed strain stabilization of the 4-node quadrilateral with 1-point quadrature for nonlinear problems. Comput Methods Appl Mech Eng 54:279–301
9. Reese S, Wriggers P, Reddy BD (2000) A new locking-free brick element technique for large deformation problems in elasticity. Comput Struct 75:291–304
10. Reese S, Wriggers P (2000) A new stabilization concept for finite elements in large deformation problems. Int J Numer Methods Eng 48:79–110
11. Simo JC, Armero F (1992) Geometrically non-linear enhanced strain mixed methods and the method of incompatible modes. Int J Numer Methods Eng 33:1413–1449
12. Taylor RL, Beresford PJ, Wilson EL (1976) A non-conforming element for stress analysis. Int J Numer Methods Eng 10:1211–1219
13. Hueck U, Wriggers P (1995) A formulation for the four-node quadrilateral element, part i: Plane element. Int J Numer Methods Eng 38:3007–3037
14. Wriggers P, Hueck U (1996) A formulation of the enhanced qs6-element for large elastic deformations. Int J Numer Methods Eng 39:3039–3053
15. Loehnert S, Boerner EFI, Rubin MB, Wriggers P (2005) Response of a nonlinear elastic general Cosserat brick element in simulations typically exhibiting locking and hourglassing. Comput Mech 36:255–265
16. Boerner EFI, Loehnert S, Wriggers P (2007) A new finite element based on the theory of a Cosserat point - Extension to initially distorted elements for 2D plane strain. Int J Numer Methods Eng 71:454–472
17. Rubin MB, Jabareen M (2007) An improved 3-D brick Cosserat point element for irregular shaped elements. Comput Mech 40(6):979–1004
18. Camacho GT, Ortiz M (1996) Computational modeling of impact damage in brittle materials. Int J Solids Struct 33:2899–2938
19. Guo Y, Ortiz M, Belytschko T, Repetto EA (2000) Triangular composite finite elements. Int J Numer Methods Eng 47:287–316
20. Thoutireddy P, Molinari JF, Repetto EA, Ortiz M (2002) Tetrahedral composite finite elements. Int J Numer Methods Eng 53:1337–1351
21. Rubin MB, Jabareen M (2007) A 3D brick macro-element for nonlinear elasticity. Comput Mech (Submitted)
22. Simo JC, Hughes TJR (1986) On the variational foundations of assumed strain methods. J Appl Mech 53:51–54
23. Flory PJ (1961) Thermodynamic relations for high elastic materials. Trans Faraday Soc 57:829–838
24. Simo JC, Armero F, Taylor RL (1993) Improved versions of assumed enhanced strain tri-linear elements for 3D finite deformation problems. Comput Meth Appl Mech Eng 110:359–386
25. Crisfield MA, Moita GF, Jelenic G, Lyons LPR (1995) Enhanced lower-order element formulations for large strains. Comput Mech 17:62–73
26. Crisfield MA, Moita GF (1996) A co-rotational formulation for 2-D continua including incompatible modes. Int J Numer Methods Eng 39:2619–2633
27. Moita GF, Crisfield MA (1996) A finite element formulation for 3-D continua using the co-rotational technique. Int J Numer Methods Eng 39:3775–3792